

ARES: a versatile benchtop testbed for evaluating techniques for imaging through atmospheric turbulence

Caleb Abbott¹, Daniel Johns¹, Fabien R. Baron¹,
Stuart M. Jefferies^{1,8}, Deborah J. Gulledge¹, Cody L. Shaw⁴,
Fallon P. Konow¹, Dmitriy Shcherbik¹, Arturo O. Martinez³,
Caytyn Abono², Lewis C. Roberts Jr.⁵, Ryan Swindle⁶,
and Douglas A. Hope^{7,1}

¹ Georgia State University; ² University of California, Berkeley;

³ NASA Ames Research Center; ⁴ Air Force Research Laboratory;

⁵ Jet Propulsion Laboratory, California Institute of Technology;

⁶ USSF; ⁷ Georgia Tech. Research Institute;

⁸ University of Hawai'i

Abstract

The Advanced Reconnaissance of Earth-orbiting Satellites (ARES) simulator is a test bed for the validation of novel methods for high-resolution, ground-based imaging of targets in the near-Earth environment. It is currently supporting research and research-related education into innovative methods for imaging through atmospheric turbulence: a critical research area for Space Domain Awareness. An additional function of the ARES system is to facilitate the transitioning of our research into operational assets for the Department of Defense. Here we provide an overview of the current status of ARES and its capability, and we discuss future extensions and applications.

1 Background

Ground-based observations of objects in the volume of space from low-Earth orbit (LEO) to Cislunar play a pivotal role in Space Domain Awareness (SDA). All observations, however, suffer degradation due to turbulence in the Earth's atmosphere. Therefore, the government and private industry have invested significant effort and resources to mitigate the adverse effects of atmospheric turbulence. The *Advanced Reconnaissance of Earth-orbiting Satellites* (ARES) instrument is a versatile benchtop platform for simulating atmospheric turbulence. ARES can

be used for testing and calibrating prototype instrumentation for on-sky development, and validating techniques and ideas developed theoretically or through numerical simulations in research for imaging through atmospheric turbulence.

In addition to providing a research tool and testbed for novel techniques for ground-based imaging of near-Earth orbiting satellites, ARES also provides an educational tool for training the next generation of scientists in advanced methods for high-resolution imaging. Students (graduate and undergraduate) and postdocs can use ARES to gain practical “hands-on” experience with optics and engage in state-of-the-art research projects that impact SDA and astronomy. Here we describe the architecture of the ARES simulator and provide examples of its use for research.

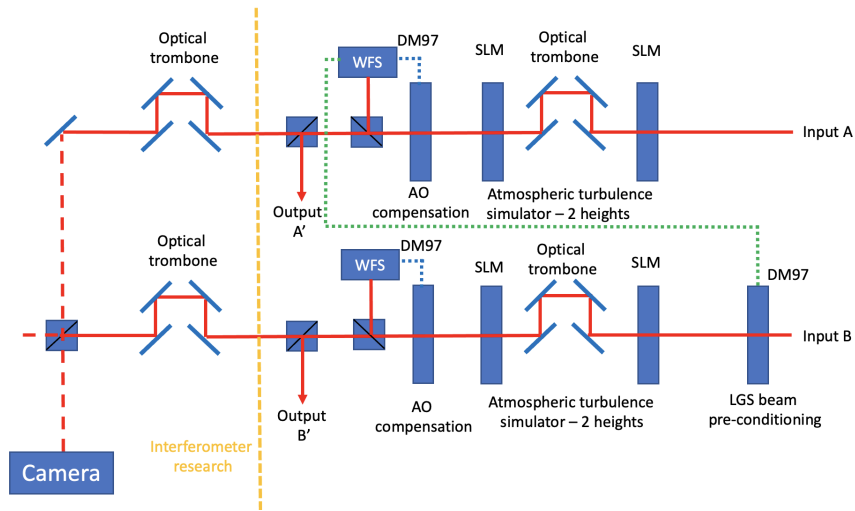


Figure 1: This figure shows a schematic of ARES configured for conducting research into the projects described in Section 3.1. Here DM97 and WFS represent a deformable mirror (DM) with 97 actuators and a Shack-Hartmann wavefront sensor from ALPAO, and SLM is a spatial light modulator from Meadowlark. LGS represents the “laser guide star” channel with pre-conditioning of the beam. The blue dotted line is for the WFS when used in closed loop with the DM in channel A. The green dotted line is for the WFS when used in the open loop with the DM in channel B. The hardware to the left of the vertical orange dashed line is used for interferometry experiments and demonstrations.

ARES can be thought of as an “optics Lego kit” comprised of deformable mirrors, Shack-Hartmann wavefront sensors, spatial light modulators (SLMs), a wide range of optics and optomechanics, and multiple software tools and packages to control and operate active elements of a testbed. The details of the hardware are given in the Appendix. ARES is designed to be reconfigured with “minimal” effort to provide a versatile testbed for novel techniques for imaging

through atmospheric turbulence. Figure 1 shows a schematic of the current ARES configuration.

2 Turbulence generation

2.1 Phase screen generation

We generate static phase screens using a standard Fourier transform power spectrum filter function approach. First we create a 2D complex array of random numbers where the real and imaginary components of the array are generated from a Gaussian distribution with mean = 0 and standard deviation $\sigma = 1$. Second, we multiply this array by the amplitude of the wavefront phase spectral density given by

$$A_\phi(i, j) = 0.151 (2D/r_0)^{5/6} (i^2 + j^2)^{-11/12}. \quad (1)$$

where i and j are the sample indices, D is the diameter of the telescope aperture, and r_0 is the Fried parameter [1]. Third, we set the D.C. (i.e. zero spatial frequency) bin to zero to ensure a zero mean phase at the end of the process. Fourth, we inverse Fourier Transform the resultant array to produce two independent realizations of a Kolmogorov phase screen: one in the real part of the transform, the other in the imaginary part. We note that for the simulated screen to be accurate over the aperture we are interested in we need to generate the screen on an array that is at least four-times larger than the aperture. This is necessary for two reasons. First, we need to use a number of points in the simulation that can capture the outer scale length of the turbulence L_0 which typically has a value of around 15 to 25 m, depending upon the site [2]. Without this, the low spatial frequencies are not adequately represented and the observed phase structure function for the phase screen does not well represent the expected phase structure function

$$D_\phi(\rho) = 6.88 \left(\frac{|\rho|}{r_0} \right)^{5/3}. \quad (2)$$

Here $|\rho|$ is the spatial length scale between points in the phase screen. Second, using the Fast Fourier Transform (FFT) approach for generating a phase screen results in phase screens that are periodic in x and y and which do not appear to have any apparent overall slope. This is not realistic. However, the shortcoming can be mitigated by only using the central section of the screen.

A wavefront evolves both spatially and temporally. This results in spatial and temporal correlations in a set of wavefronts that are measured over an interval that is commensurate with, or less than, the atmospheric coherence time

$$\tau_0 = 0.314 r_0 / \bar{V}, \quad (3)$$

where \bar{V} represents a weighted average of the wind velocity over the height range of the turbulence.

We use the approach of Dayton et al. [3] to capture the spatial and temporal correlation behavior in the wavefront. In their approach the primary spatial evolution is near frozen flow translation due to wind speed. After translating the phase screen to account for the frozen flow behavior, the shifted phase screen is updated with a new phase screen generated with an independent array of complex numbers, using the auto-regressive average algorithm

$$\Phi_{update} = \alpha\Phi_{shift} + (1 - \alpha)\Phi_{new} \quad (4)$$

where α is the auto-regressive parameter. This parameter dictates the level of temporal and spatial evolution in the wavefront.

2.2 Optical set up

Figure 2 shows a schematic of our current optical setup for a two-layer turbulence module¹.

One layer is located in the entrance aperture. The height of the second layer can be varied using an optical trombone. Here, in order to provide realistic propagation, we need to preserve the Fresnel number defined by

$$F_n = \frac{D_s^2}{\lambda z_s} = \frac{D_A^2}{\lambda z_A} \quad (5)$$

[3], where λ is the wavelength of the light, D_s and D_A are the physical diameters of the aperture we want to simulate and the aperture in ARES, respectively, and z_s and z_A the corresponding propagation distances. We use precision Zaber linear translation stages in our optical trombones, which allow for $z_A \leq 15$ cm. Using Eqn. 5 we can see that for $D_s=3.6$ m and $D_A=0.01$ m, we can simulate a propagation range of up to ~ 19 km.

To take account for non-uniformity in the optical flatness of each SLM display and the aberrations in the lenses ahead of them, we acquire a set of phase-diverse image data from each SLM.

These phase-diverse data are then used in a phase retrieval algorithm to recover the total aberration at the face of each SLM. These static phase errors are recovered by minimizing the cost function

$$\epsilon = \sum_k \sum_{\mathbf{x}} (g_k(\mathbf{x}) - \hat{g}_k(\mathbf{x}))^2 \quad (6)$$

where $g(\mathbf{x})$ is the observed image and $\hat{g}(\mathbf{x})$ is a model of the image given by

$$\hat{g}_k(\mathbf{x}) = |FT^{-1}\{A_k(\mathbf{u})\}|^2 \quad (7)$$

with

$$A_k(\mathbf{u}) = |A|e^{j[(\phi(\mathbf{u}) + \theta_k(\mathbf{u}))]} \quad (8)$$

¹We can model up to nine layers using our suite of SLMs.

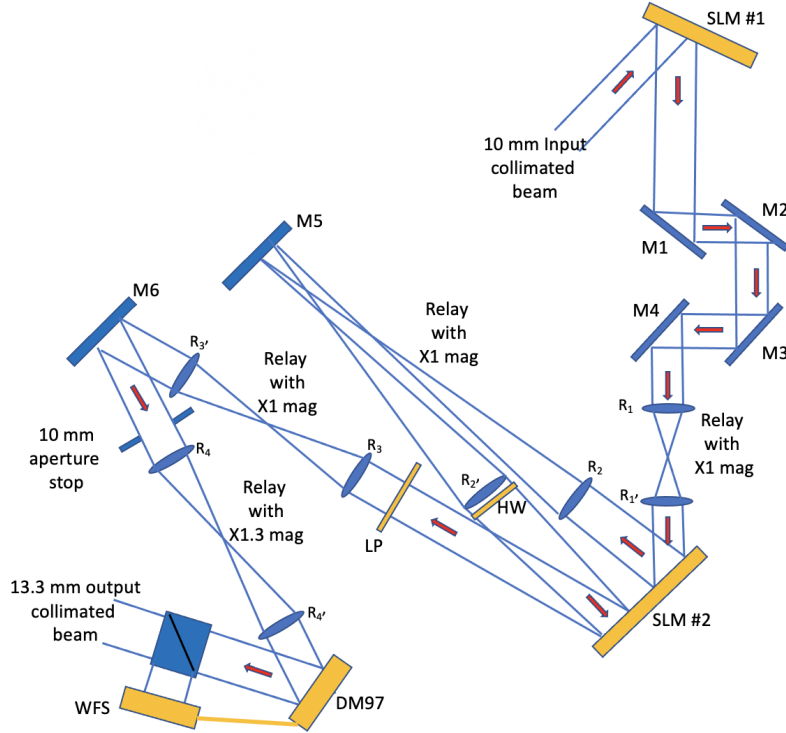


Figure 2: This figure shows a schematic of the two-layer atmospheric turbulence module followed by the adaptive optics module. The angle of incidence for the input beam onto an SLM is kept less than 10 degrees.

Here $\phi(\mathbf{u})$ is the unknown static aberration, $\theta(\mathbf{u})$ is a known ‘‘diversity phase’’ added to the SLM, $|A|$ is a uniform pupil mask normalized such that the volumes of \hat{g} and g are equal, FT^{-1} is an inverse Fourier transform, and $j = \sqrt{-1}$.

To estimate the phase aberration accurately, we used a range of Zernike modes, including defocus, astigmatism, and coma, for the diversity phases. These different diversity phases, which are represented by the index k , are each applied as a bisymmetric pair [13,14]. The variables in the minimization are the pixels in the array that defines $\phi(\mathbf{u})$.

Figure 3 shows images of a point source as measured after a single layer of turbulence. Similar results are obtained for both layers. This figure shows that as the level of turbulence increases, a bright spot appears at the center of the image. This spot, known as the zero-order diffraction spot (ZODS), is due to light that is not modulated by the pixels on the SLM: e.g., the light reflected from between the pixels.

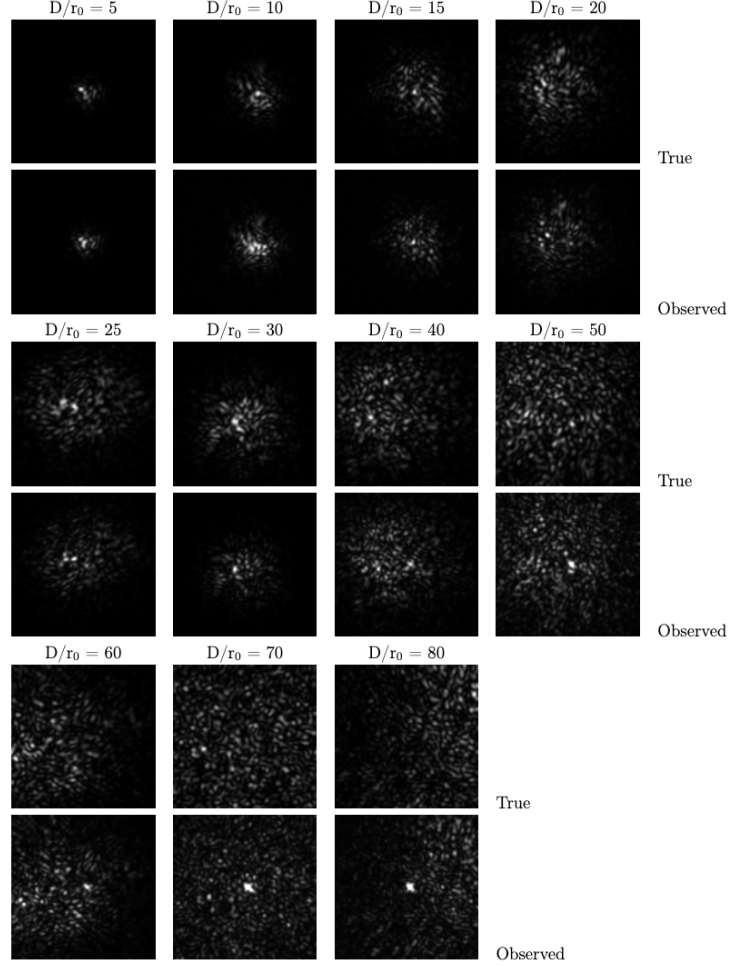


Figure 3: This figure shows the high-fidelity of the atmospheric point spread functions produced by each SLM in the ARES turbulence simulator over a wide range of atmospheric turbulence conditions as measured by the ratio D/r_0 ; where D is the diameter of the telescope aperture and r_0 is the atmospheric coherence length for the observations. The first, third, and fifth rows of images show the expected PSFs determined from numerical simulations. The second, fourth, and sixth rows of images show the corresponding PSFs generated by ARES. All images are on a linear scale. A zero-order diffraction spot can be seen in the centers of the images for $D/r_0 > 40$. This spot is removed through polarization control (see main text). We note that the images in this figure were obtained without the second pass from SLM#2, i.e. lenses R_2 and $R_{4'}$ provided the final 4 f relay system to the deformable mirror. Also, there is a difference in magnification between the true and observed images. When recording the image sequences, we adjusted the brightness of the source for each exposure so as to fill the camera's dynamic range.

The visibility of the ZODS increases as the level of turbulence increases. This is because the amplitudes of the speckles become commensurate with the amplitude of the ZODS as the number of speckles in the PSF increases ($N_{speckles} \sim (D/r_0)^2$).

There are a few ways to mitigate the presence of the ZODS, including 1) adding a blazed grating on the SLM to separate the zero and first-order light on the focal plane, allowing the use of an aperture to remove the ZODS, 2) adding defocus to the SLM so that the ZODS becomes diffuse in the image plane, 3) replacing a physical lens in the 4F-system after the SLM with a Fresnel lens function on the SLM, and 4) using the SLM to manipulate the polarization of the beam such that only light modulated by the pixels can pass through a linear polarizer located after the SLM.

The first approach doesn't provide enough separation when the level of turbulence results in a broad speckle pattern. The second approach, which is shown in Fig. 4, results in limitations if the output beam from the turbulence generator is to be used for testing wavefront sensors or with adaptive optics systems: the ZODS affects the quality of the wavefront estimate provided to the deformable mirror by the Shack-Hartmann wavefront sensor. The third approach reduces the fidelity between the computed ("synthetic") PSF and the PSF generated by the SLM. This reduction in image quality when using a Fresnel lens is well known. This leaves us with approach (4).

Here we use a split screen configuration on the simulator's second SLM and a second pass to provide a polarization modulation of the beam (see Fig. 2). This modulation is achieved through a half-wave plate located before the second half of the input screen and a linear polarizer after the SLM. The half-wave plate is oriented to re-align the incoming polarization to 45 degrees to the slow axis of the SLM. The linear polarizer is arranged to have its polarization axis orthogonal to that of the incoming beam. A phase change of π radians added to the light reflected from the pixels of the SLM causes the polarization to be rotated by 90 degrees: thus allowing passage through the linear polarizer. The ZOD light, on the other hand, is extinguished.

We model the turbulence screens in the ARES simulator with a resolution of ~ 4 pixels/ r_0 value. This means that for a beam size of ~ 800 pixels in diameter on the SLM, we can, in principle, generate turbulence of up to $D/r_0 \sim 200$. This represents the level of turbulence we might encounter at visible wavelengths during good seeing conditions when observing with a 30-m class telescope. However, to realize this high value of D/r_0 , the phase wraps in the holograms applied to the SLMs, must be resolvable by the number of pixels and pixel spacing of the SLMs. At high levels of turbulence, the phase wraps are densely packed.

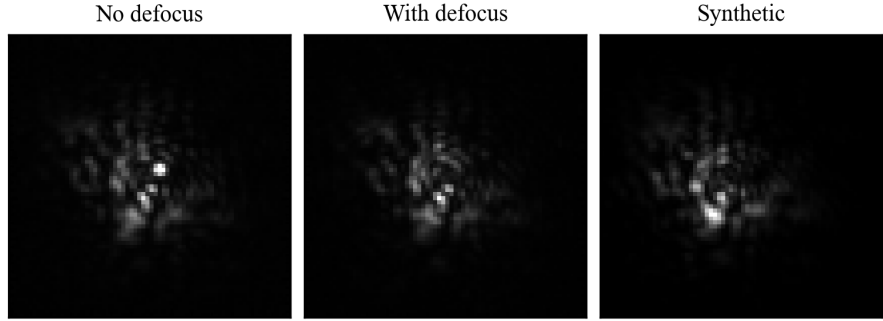


Figure 4: This figure shows the removal of the ZODS by using the defocus approach. The image on the left has the ZODS, while in the central image the ZODS is affected by 9 waves of defocus and can't be seen. The image on the right is the computed synthetic PSF for the phase screen applied to the SLM.

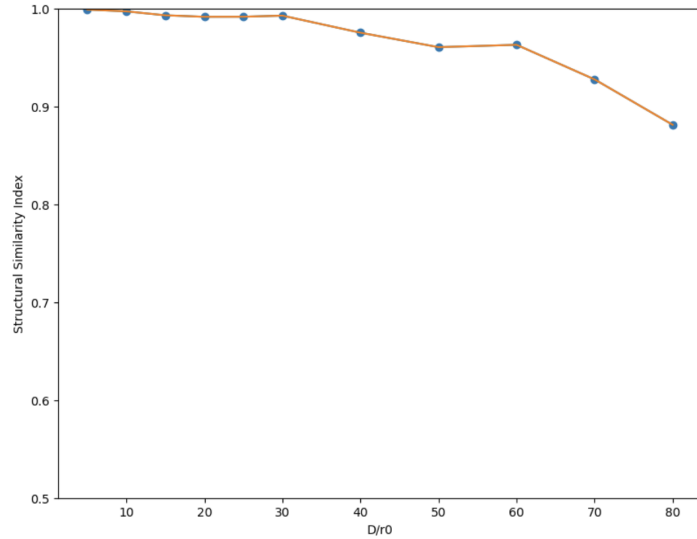


Figure 5: The SSIM values for the PSFs generated with ARES, and the synthetic PSFs generated numerically using the same phase screens. The synthetic PSFs were resized to best match the observations.

To objectively assess the quality of the PSFs generated with ARES, we use the Structural Similarity Index Measure (SSIM) [18] and measure the SSIM for the ARES images and the numerical (synthetic) images computed with the same phase screens. The SSIM is used for measuring the similarity between two

images and has a value between 0 and 1.

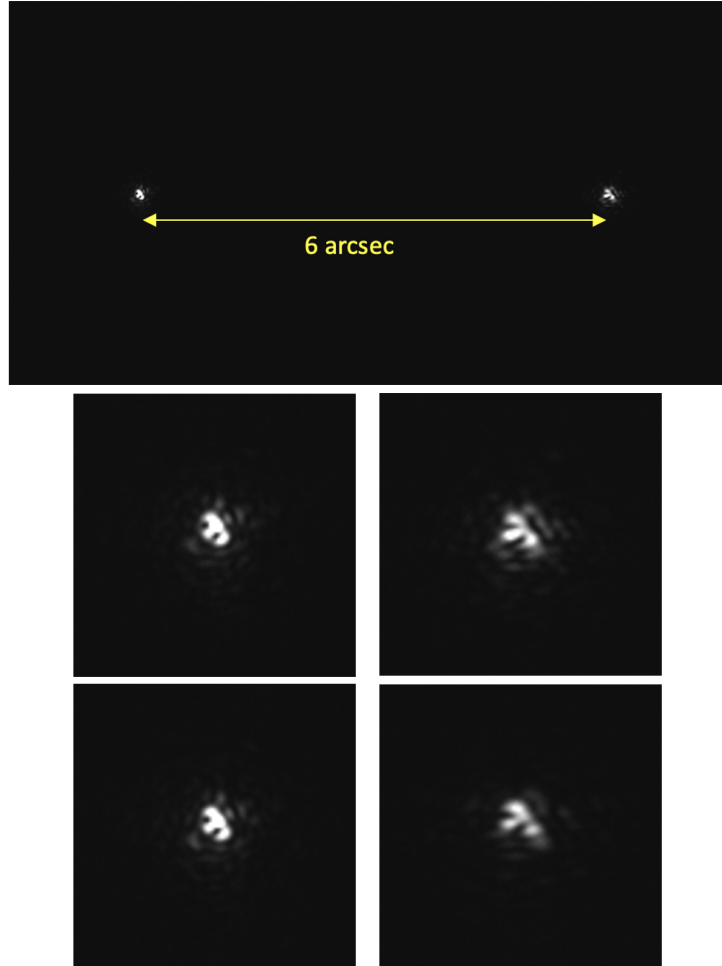


Figure 6: The image in the top row represents a $9.5 \text{ arcsec} \times 5 \text{ arcsec}$ cut-out from the full field-of-view of $22 \text{ arcsec} \times 12 \text{ arcsec}$. The magnified sub-images are taken from the top image. The sub-images in the left column for the middle and bottom rows, represent the PSFs observed when both phase screens are located in the entrance pupil (bottom row) and when one screen is moved to 19 km (middle row) for the on-axis source. The right column shows the corresponding images for the off-axis source.

A value 1 is obtained when two images are identical. A value of 0 indicates no structural similarity. Figure 5 shows high SSIM values up to $D/r_0 = 80$. For observations with the AEOS 3.6m telescope, this corresponds to the strong

turbulence that might be expected during daytime observations or at high zenith angles at visible wavelengths. In the future we will ascertain how the SSIM varies at even higher levels of turbulence and at what point the phase wrap issue discussed above starts to impact our simulations.

2.2.1 Anisoplanatic imaging:

Figure 6. shows example images of how two unresolved objects, one on-axis, the other off-axis 6 arcsec away, change when one of the turbulence layers is moved from being co-located with the other layer in the entrance aperture, to an effective height of ~ 19 km. This figure, which shows the PSF for the off-axis source changing as the height of the second layer is increased, while the on-axis PSF remains essentially unchanged (as expected), demonstrates that we can investigate the imaging of targets with large spatial extent. Our current optical setup allows for a field-of-view of 22 arcsec \times 12 arcsec.

2.3 Adaptive optics compensation

To allow for studies of speckle imaging with adaptive optics (AO) compensation, we place an AO system at the exit of each turbulence generator module. The AO system comprises a 97-actuator deformable mirror (DM), with 11 actuators across the diameter, and a Shack-Hartmann wavefront sensor (SH WFS). Figure 7 shows examples of some PSFs generated by ARES with and without AO compensation.

2.4 Object generator module

We want to be able to simulate a wide range of targets, from satellites in LEO, to unresolved closely spaced targets in geosynchronous orbits and Cis-lunar space. We are therefore developing a versatile object generator module to provide this capability. A schematic of the current version of this module is shown in Fig. 8.

We use 637 nm lasers equipped with 5 μm single-mode fibers and achromat lenses to generate three collimated beams that can be fed into the entrance aperture of the atmospheric turbulence simulator. One of the beams, which we call the “general object generator beam,” uses a reflective spatial light modulator (SLM) to manipulate the wave field of the beam:

$$A(u, v) = |A(u, v)|e^{+j\theta(u, v)} . \quad (9)$$

In principle, we can find values for $|A(u, v)|$ and $\theta(u, v)$ that can provide an image of almost *any* object, $o(x, y)$, we want, when the wave field is Fourier transformed by an objective lens and imaged onto a camera. We determine the necessary values for $|A|$ and θ by minimizing the error metric

$$\epsilon_0 = \sum_{x,y} r(x, y)r^*(x, y) , \quad (10)$$

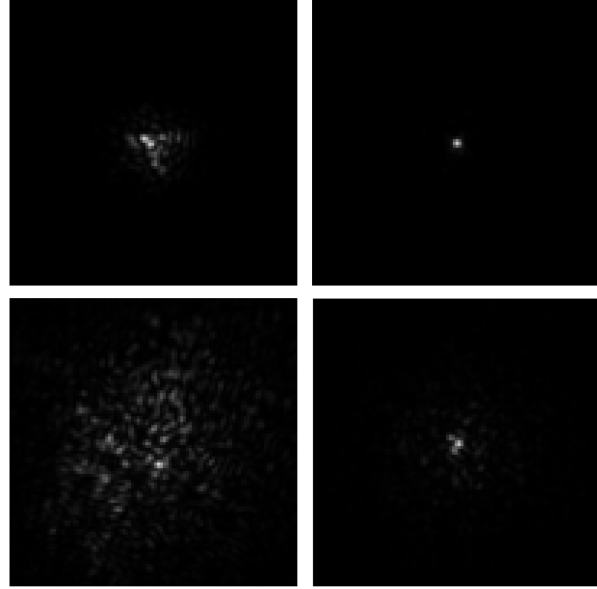


Figure 7: PSFs generated with two phase screens, co-located in the entrance aperture, without (left column) and with AO compensation (right column) for $D/r_0 = 7$ (top row) and 30 (bottom row). The ZODS is not removed from the these 100×100 pixel images.

where

$$r(x, y) = o(x, y) - a(x, y)a^*(x, y), \quad (11)$$

$a(x, y)$ and $A(u, v)$ are a Fourier transform pair, and $*$ denotes complex conjugate.

To modulate both θ and $|A|$ of the complex wave field in the beam requires two reflections off the SLM: one to modulate θ , and one to modulate $|A|$. The latter can be achieved in one of two ways. The first way uses a half-wave plate to align the polarization of the beam to be at 45 degrees to the polarization axis of the SLM. This configuration allows the SLM to rotate the polarization of the beam through phase modulation. A linear polarizer placed downstream of the SLM then acts as a polarization analyzer that reduces the amplitude of the reflected beam according to the degree of rotation introduced by the SLM [17]. We note the performance of this approach to modulating $|A|$ is reported to suffer from limitations incurred by the discretization of the phase modulation into 8-bits [15].

The second way to generate the required amplitude distribution, which is free of the discretization effects for the first method, uses a second phase modulation [15]. Here we determine the two required phase maps, β and ψ , by minimizing

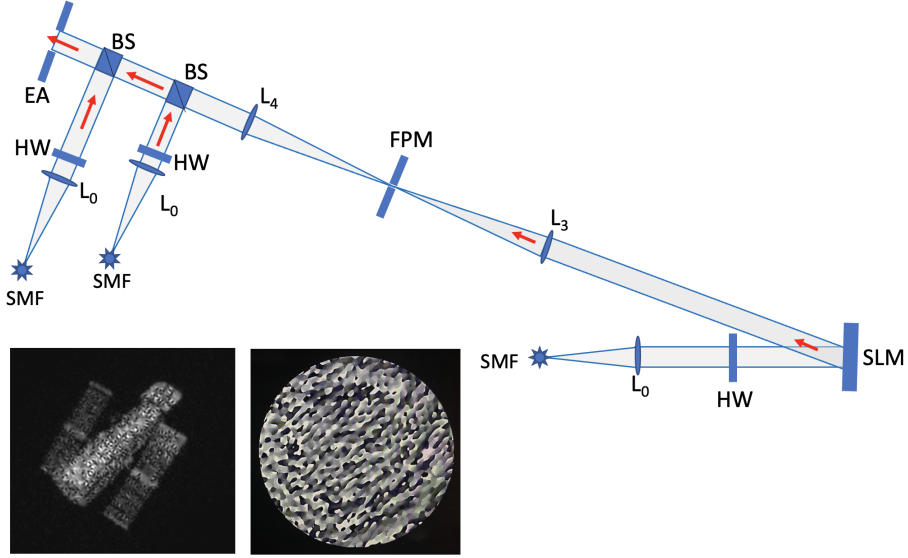


Figure 8: A schematic of the ARES object generator module. An achromat lens L_0 collimates the light from a linearly polarized 637 nm laser with a 5-micron single mode fiber (SMF) in each of three beams. A half-wave plate (HW) in each beam then orients the polarization from the SMF to minimize the intensity of the zero order diffraction spots from downstream spatial light modulators (SLMs). FPM is a focal plane mask that removes the zero-order diffraction spot from the “general object generator beam”. BS are beam splitters, and EA is the entrance aperture to the atmospheric turbulence generator. The images at the bottom show the phase screen input to the SLM in the “general object generator beam” (right) and the resultant image of the Hubble Space Telescope at the location of the FPM (left).

Eqn. 10 with

$$a(x, y) = FT \left[\alpha(u, v) e^{+j\beta(u, v)} \right] \quad (12)$$

and

$$\alpha(u, v) = FT \left[|B(x', y')| e^{+j\psi(x', y')} \right] \quad (13)$$

where $|B|$ is the amplitude of the input beam and $FT []$ denotes the Fourier transform operator. We note, however, that the optical setup for this approach is very sensitive to alignment errors [17].

Because of the above mentioned practical issues with both methods for producing amplitude variations in the beam, we investigated the performance of a setup with a single, phase-only, modulation by the SLM (see Fig. 8). Here, we minimize Eqn 10 with $|A|$ set to the square root of the measured intensity of

the pupil image and only θ is allowed to vary in the minimization.

We found that although the single phase approach provides good quality images of simple objects, it leads to artifacts in more complex images. For example, Fig. 8 shows the realization of a phase-only solution for the Hubble Space Telescope. The image demonstrates a high level of "speckling." As this level of artifact is too high for our proposed studies, we will be updating our general object generator beam for full complex manipulation.

Although full complex modulation of the beam can replicate most objects of interest for our research, for investigations into the detection of closely spaced (unresolved) objects (CSOs), where the contrast between the two sources is greater than 100:1, we are unable to find a numerical solution for $|A|$ and θ , or ψ and β , than can replicate both point sources. As we are interested in CSOs with much larger contrast ratios, we need to turn to the other two beams in our object generator. Here the single mode fibers are mounted on x-y translation stages so that we can model two unresolved sources at different separations. With this setup we can extend our contrast ratio to $\sim 100,000:1$.

3 Research Projects

3.1 Monochromatic imaging

ARES is currently supporting a number of research projects on imaging through turbulence using monochromatic light. The main project at the time of this paper is "Simulating Turbulence for Uplink Laser Compensation Experiments" (see Fig. 9). In laser communications, the uplink laser passes through the Earth's turbulent atmosphere on the way to the spacecraft. This causes the beam to break up and suffer deep fades. Pre-compensating the beams with adaptive optics (AO) can remove the effects of the turbulence.

Testing these AO systems in the lab is difficult because traditional phase wheel turbulence simulators [10], cannot simulate the partially correlated turbulence conditions that the downlink and the uplink experience due to the motion of the spacecraft. The spatial light modulators that are used to simulate atmospheric turbulence in the ARES system do not have this limitation.

Other projects underway by our group that are using, or will soon use, the ARES configuration shown in Fig. 1 include:

- Imaging through strong turbulence (low elevation angles, daytime conditions) [5]
- High-resolution high-contrast imaging of closely spaced objects [6]
- Imaging over a wide-field-of-view [5]
- High-fidelity wavefront sensing [5]
- PSF Engineering using the Hybrid Optical Telescope concept [16]
- Dynamic aperture diversity [11]

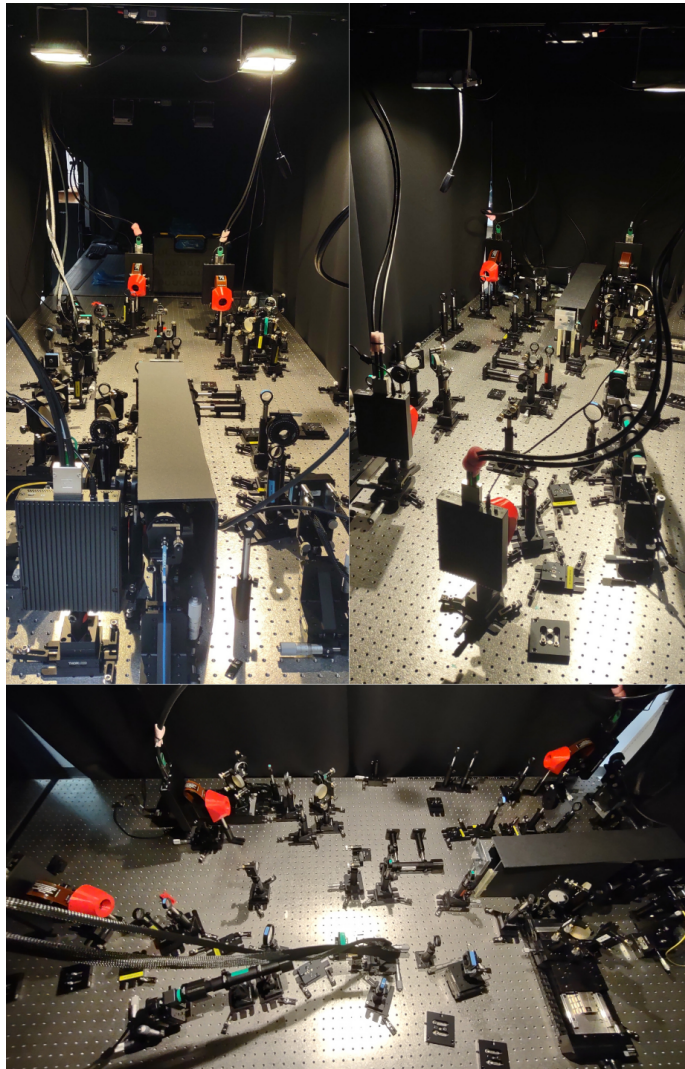


Figure 9: These images show ARES configured for the JPL satellite communications project.

3.2 Polychromatic imaging

We are also developing a polychromatic turbulence simulator module for ARES. This system will comprise of two layers of atmospheric turbulence, modeled using deformable mirrors with 242 actuators, followed by AO compensation with an AO system with a deformable mirror with 242 actuators. The primary use for this configuration is to support our research into hyper-spectral broadband

speckle imaging [12].

3.3 Other potential configurations

The components in ARES can be rearranged into systems to support other research of interest to the Department of Defense. Two examples are imaging through volume turbulence (i.e., over large horizontal paths), and imaging with multi-conjugate adaptive optics. For the former we can simulate up to nine layers of turbulence with our suite of SLMs. For the latter we can simulate three-layer compensation using a woofer-tweeter configuration (i.e. 97 and 242 actuator DM pairs) for each layer.

Acknowledgements

Funding for the ARES simulator was provided by the Air Force Office of Scientific Research (AFOSR) through awards FA9550-18-1-0411 and FA9550-21-1-0155 under the Defense University Research Instrumentation Program (DURIP). D.J., F.P.K, and D.S. were supported by AFOSR award FA9550-21-1038. Caytyn Abono acknowledges support from the National Science Foundation's Research Experiences for Undergraduates program under Grant No. 2050829 to Georgia State University. D.J.G. was supported by the AFRL Scholars Program and NSF Grant No. 1937956. A portion of this research was carried out at the Jet Propulsion Laboratory, California Institute of Technology, under a contract with the National Aeronautics and Space Administration (NASA).

References

- [1] R. Lane, A. Glindemann and J. C. Dainty 1992, “Simulation of a Kolmogorov phase screen,” Waves in Random Media, 2, 209-224
- [2] G. Sedmak 2004, “Implementation of Fast-Fourier-Transform-Based Simulations of Extra-Large Atmospheric Phase and Scintillation Screens,” Applied Optics, 43, 4527-4538
- [3] D. Dayton, M. Spencer, A. Hassall, and T. Rhoadarmer 2018, “Distributed-volume optical disturbance generation in a scaled laboratory environment using nematic liquid-crystal phase modulators,” Unconventional and Indirect Imaging, Image Reconstruction, and Wavefront Sensing 2018, edited by Jean J. Dolne, Philip J. Bones, Proc. of SPIE Vol. 10772, 107720H
- [4] N. Miura 2003, “Blind deconvolution under band limitation”, Optics Letters, 28 (23), pp. 2312 - 2314
- [5] D. Hope, S. M. Jefferies, M. Hart and J. Nagy 2016, “High-resolution speckle imaging through strong atmospheric turbulence.” Opt. Express 24(11), 12116–12129

- [6] D. A.Hope, S. M. Jefferies, F. Pedichini, G. L. Causi, M. Mattioli and S. Antoniucci 2019, “High-resolution, high-contrast, imaging of small objects near satellites.” In: Proceedings of the Advanced Maui Optical and Space Surveillance Technologies Conference, Maui Economic Development Board, Kihei, HI, p id.2
- [10] S. Mantravadi, T. Rhoadarmer, and R. Glas 2004, “Simple laboratory system for generating well controlled atmospheric-like turbulence”, Advanced Wavefront Control: Methods, Devices, and Applications II. Edited by Ginglewski, John D.; Gruneisen, Mark T.; Giles, Michael K. Proc. of the SPIE, Vol. 5553, 290-300
- [11] S. M. Jefferies, A. Knox, A. Dhada, C. Abbott and D. A. Hope 2017, “Dynamic aperture diversity”, AMOS Conference, Wailea, Maui September 19-22, 2017, id.92
- [12] R. Hall and S. M. Jefferies 2022, “Hyper-Spectral Speckle Imaging for Space Situational Awareness,” The Journal of the Astronautical Sciences, 69, 581–592
- [13] S. M. Jefferies, M. Lloyd-Hart, E. K. Hege, and J. Georges 2002, ”Sensing wave-front amplitude and phase with phase diversity,” Applied Optics, 41 (11), 209
- [14] P. Zhang, C. Yang, Z. Xu, Z. Cao, Q. Mu and L. Xuan 2017,”High-accuracy wavefront sensing by phase diversity technique with bisymmetric defocuses diversity phase,” Sci Rep 7, 15361
- [15] A. Jesacher, C. Maurer, A. Schwaighofer, S. Bernet and M. Ritsch-Marte 2008, ”Near-perfect hologram reconstruction with a spatial light modulator,” Optics Express, 16(4), 2597
- [16] M. Langlois, C. Graf, G. Moretto, J. R. Kuhn, I. Cunningham, S. Jefferies, K. Lewis, N. Lodieu, M. Loupias, R. Rebolo, R. Swindle, Ye Zhou 2022, ”Small-ELF project: Performance of an extreme adaptive optics system compensating for atmospheric turbulence, cophasing a diluted pupil and performing dark hole coronography in order to reach high contrast exoplanet direct detection”, SPIE Proceedings Volume 12182, Ground-based and Airborne Telescopes IX; 121820G
- [17] M-L. Hsieh, M-L. Chen, and C-J. Cheng 2007”Improvement of the complex modulated characteristic of cascaded liquid crystal spatial light modulators by using a novel amplitude compensated technique,” Optical Engineering, 46(7), 070501-1
- [18] Wang, Z. Bovik, A.C., Sheikh, H.R., Simoncelli, E.P. 2004 ”Image quality assessment: from error visibility to structural similarity”. IEEE Transactions on Image Processing. 13 (4): 600–612

Appendix

ARES Hardware

- *SLMs:* Liquid Crystal on Silicon (LCoS) reflective SLMs with 1152 x 1920

pixels and $9.2 \mu\text{m}$ pixels from Meadowlark. Four high-speed models (555 Hz) and two medium speed models (83 Hz)

- *Deformable mirrors:* Three DM241 mirrors (241 actuators) and three DM97-15 mirrors (97 actuators) from ALPAO; one Kilo DM (1024 actuators) from Boston Micromachines
- *Wavefront sensors:* Six high-speed Shack-Hartmann sensors from ALPAO; one Shack-Hartmann sensor from Thorlabs
- *Cameras:* Three Zyla 5.5 sCMOS cameras from Andor, $6.5 \mu\text{m}$ pixels, 2560x2160 pixel array, QE = 0.64 at 637 nm, 49 fps @ 16-bit; one Prime 95B sCMOS camera from Photometrics, $9 \mu\text{m}$ pixels, 1200x1200 pixel array, QE = 0.95 at 637 nm, 40 fps @ 16-bit